Effect of Additively Manufactured Sphene Ceramic Scaffolds on Bone Response in Rat Critical-Size Calvarial Defects

Giulia Brunello, Hamada Elsayed, Lucia Schiavon, Elia Sbettega, Giovanna Iezzi, Barbara Zavan, Simone Carmignato, Enrico Bernardo, Lisa Biasetto, Stefano Sivolella

applied sciences

MDPI

Article

Effect of Additively Manufactured Sphene Ceramic Scaffolds on Bone Response in Rat Critical-Size Calvarial Defects

Giulia Brunello [1,2,3], Hamada Elsayed [4], Lucia Schiavon [2,5,*], Elia Sbettega [6], Giovanna Iezzi [7], Barbara Zavan [8], Simone Carmignato [6], Enrico Bernardo [4], Lisa Biasetto [4] and Stefano Sivolella [2]

1 Department of Oral Surgery, University Hospital of Düsseldorf, 40225 Düsseldorf, Germany; giulia.brunello@med.uni-duesseldorf.de
2 Department of Neurosciences, School of Dentistry, University of Padova, 35122 Padova, Italy; stefano.sivolella@unipd.it
3 Department of Orthodontics and Dentofacial Orthopaedics, Charité—Universitätsmedizin Berlin, Corporate Member of Freie Universität Berlin and Humboldt-Universität zu Berlin, 10117 Berlin, Germany
4 Department of Industrial Engineering, University of Padova, 35122 Padova, Italy; hamada.elsayed@unipd.it (H.E.); enrico.bernardo@unipd.it (E.B.); lisa.biasetto@unipd.it (L.B.)
5 Clinic of Reconstructive Dentistry, Center of Dental Medicine, University of Zurich, 8006 Zurich, Switzerland
6 Department of Management and Engineering, University of Padova, 36100 Vicenza, Italy; sbettegaelia@gmail.com (E.S.)
7 Departement of Medical, Oral and Biotechnological Sciences, University "G. d'Annunzio" of Chieti-Pescara, 66013 Chieti, Italy; gio.iezzi@unich.it
8 Medical Sciences Department, University of Ferrara, 44121 Ferrara, Italy; zvnbbr@unife.it
* Correspondence: lucia.schiavon@zzm.uzh.ch

Abstract

Silica-based bioceramics are promising bone substitutes with tunable degradation and mechanical properties. We aimed to assess bone response in critical-size calvarial defects in rats, empty or filled with 3D-printed sphene ceramic ($CaTiSiO_5$) scaffolds produced using direct ink writing from preceramic polymers and reactive fillers. Scaffold characterization was performed using scanning electron microscopy, X-ray diffraction, porosity analysis, and compressive strength testing. Bilateral cylindrical 5 mm calvarial defects were created in 20 rats: one was randomly filled with sphene scaffold, while the contralateral remained empty. Ten animals were killed at 4 weeks, the rest at 8 weeks. Specimens were collected for micro-X-ray computed tomography (micro-CT) analysis, followed by undecalcified histology. The scaffolds exhibited porous structure with complete sphene phase purity and compressive strength of 17.91 MPa (SD 4.6). In vivo, no adverse event was noted during healing. Overall bone regeneration—as measured by BV/TV—was comparable between groups: Bone volume/total volume (BV/TV) increased over time in the empty and sphene groups, reaching ~40%, with no significant differences between groups or time points. BV/TV was significantly higher in the external regions of the defects compared to the internal areas in both groups at the two time points. The sphene group showed a significantly greater volume of new bone extending beyond the original cortical boundary at both 4 and 8 weeks ($p = 0.013$). In the sphene group histology revealed partial bone ingrowth within the scaffold, while bone in the control group was limited to defect edges. After 8 weeks, new bone adjacent to the cortical surface was thicker in the sphene group ($p < 0.05$). These initial findings are consistent with prior preclinical studies, supporting the biocompatibility and osteoconductive nature of sphene ceramic scaffolds.

Keywords: scaffold; sphene; bioactive ceramic; direct ink writing; bone regeneration

Academic Editor: Georgios Romanos

Received: 16 February 2026
Revised: 18 March 2026
Accepted: 23 March 2026
Published: 24 March 2026

1. Introduction

Significant advancements in bone augmentation have been achieved over the past decades in terms of surgical techniques and biomaterials [1,2]. Nevertheless, the reconstruction of extensive bone defects in the maxillofacial region still represents a major challenge [3,4].

A broad range of bone substitutes has been employed to date, including grafting materials of both natural and synthetic origin [1,2,5]. While autogenous bone graft is widely regarded as the "gold standard" for bone regeneration, its usage is constrained by issues such as supply limitations and the morbidity associated with donor site harvesting [6,7]. As an alternative, allogeneic bone grafting, sourced from either human cadavers or living donors, and xenogeneic bone substitutes are employed, despite the potential risks of rejection reactions or infection transmission [8]. To address these limitations, synthetic bone materials have been introduced.

A crucial criterion for an effective bone substitute is to have an interconnected porous structure that mimics the hierarchical structure of natural bone [9]. The use of foaming technologies (e.g., gas foaming, sacrificial template, freeze drying, gel-casting and emulsification) shows the potential to tailor the porosity at different length scales (from nano to macro), with some limitations in the control of interconnectivity degree and mechanical strength [10,11].

Furthermore, manually shaping bone grafts to fit a defect is a demanding procedure that requires considerable time and surgical expertise [12,13].

Additive manufacturing technologies provide a significant advantage by enabling the production of custom-made scaffolds tailored to specific bone defects, using patients' computed tomography (CT) scans as a starting point [4].

Several AM technologies have been utilized for the fabrication of scaffolds, including stereolithography [14], Direct Laser Printing (DLP), Selective Laser Sintering (SLS), Binder Jetting 3D Printing and Direct Ink Writing (DIW) [4,15,16].

DIW is a versatile 3D printing technology that consists of the room temperature extrusion of highly loaded inks or pastes, characterized by specific rheological behavior (Herschel and Bulkley fluids, meaning shear thinning with yield stress) that must be tuned to allow for printability and shape retention after printing. The versatility of the technology is expressed by the possibility of 3D printing a variety of materials [17,18]. More recently multi-materials 3D printing was also reported, thus leveraging the DIW potential [17]. Furthermore, it was shown that utilizing DIW allows for precise control of micro- and macro-scaffold architecture [15].

Several ceramic scaffolds have been successfully produced using DIW. Recently we proposed a calcium silica titanate, also known as sphene or titanite $CaTiSiO_5$, as a bioactive material for implant dentistry. We focused on the preceramic polymer route for the synthesis process both to realize coatings [19] on Ti-based implants and to 3D print scaffolds with tailored geometries [20].

The developed 3D-printed sphene ceramic scaffolds were produced with a controlled amount of porosity and enhanced compressive strength (ranging from 3.9 MPa to 12.7 MPa) and porosity (ranging from 59% to 74%) [21].

To the best of the authors' knowledge, 3D-printed sphene scaffolds have not previously been evaluated in vivo, and their performance in rat critical-size calvarial defects, a widely used model, offers a valuable opportunity to evaluate bone response in the presence of the scaffold. Although high compressive strength is not required in this context, the combination of controlled porosity and high mechanical properties suggests that these scaffolds could be suitable for future load-bearing applications, which will need to be tested after validation in the present animal model.

Therefore, the aim of this study was to evaluate the physical and chemical properties of 3D-printed sphene ceramic scaffolds. The in vivo bone response of 3D-printed sphene ceramic scaffolds was evaluated using a rat critical-size calvarial defect model, using micro-CT imaging followed by histological analyses.

2. Materials and Methods

2.1. Direct Ink Writing of Sphene Scaffolds

Sphene ($CaTiSiO_5$) ceramic scaffolds were manufactured by DIW using the polymer-derived ceramics (PDCs) route, with a molar proportion between the oxides constituting the material (i.e., $CaO/TiO_2/SiO_2$) of 1/1/1.

The production of the scaffolds was realized as previously described by Elsayed et al. [21]. Briefly, a commercially available preceramic silicone polymer (SILRES® MK, in powder form, polymethylsiloxane, Wacker-Chemie GmbH, München, Germany), which has a silica yield of ~84 wt% after heating in air at 1000 °C, was filled with micro-sized calcium carbonate ($CaCO_3$, ~10 µm, Industrie Bitossi, Vinci, Italy), nano-sized titanium oxide (TiO_2, ~21 nm, Evonik Degussa GmbH, Essen, Germany) and nano-sized fumed silica (FS, Aerosil R106, Evonik Degussa GmbH). The latter was utilized by 10 wt% of total SiO_2 content to provide the ink with adequate pseudoplastic behavior for DIW extrusion, as previously demonstrated [22].

In detail, the ink was produced by dissolving MK silicone resin in isopropanol with 30 vol% (Sigma-Aldrich, Saint Louis, MO, USA). Fumed silica was added, followed by the incorporation of TiO_2 and $CaCO_3$ active fillers into the silicone polymer. At each step, the mixture was first mixed manually and, subsequently, using a planetary mixer (THINKY ARE-250, Intertronics, Kidlington, UK) at 2000 rpm (initially for 3 min 30 s, for 3 min after adding FS, for 2 min after the addition of TiO_2 and finally for 3 min 30 s after incorporating $CaCO_3$). Then, the ink was degassed for 3 min at 2000 rpm, to remove the air bubbles entrapped. In this way, it was possible to obtain homogenous ink without traces of powder aggregates or air bubbles. The composition of the ink, with the addition of 1.7 g of isopropanol, was 3.28 g/0.31 g/4.07 g/5.11 g of $MK/FS/TiO_2/CaCO_3$, respectively.

Rheological measurements were carried out using a plate–plate rheometer (d = 40 mm, Kinexus, Netzsch, Selb, Germany), with isopropyl alcohol employed as a solvent trap to minimize evaporation. Amplitude sweep tests were performed in stress-controlled mode to evaluate the variation of complex viscosity as a function of the applied shear stress. The yield stress was defined as the stress corresponding to 95% of the zero-shear viscosity. The applied shear stress range varied according to the ink formulation, spanning from 0.1 Pa to 1000 Pa, while the oscillation frequency was fixed at 0.5 Hz.

Thixotropic behavior was subsequently evaluated to determine the structural recovery time of the mixtures. The test consisted of three sequential phases: (i) 30 s at a low stress of 0.1 Pa, (ii) 30 s at a high stress of 100 Pa, and (iii) 600 s again at 0.1 Pa.

During the first phase, the mixture subjected to a low stress (0.1 Pa) exhibited solid-like behavior characterized by high viscosity. When a higher stress (100 Pa) was applied, the ink flowed with significantly lower viscosity, behaving as a liquid. Upon returning to the low stress condition (0.1 Pa), the internal structure gradually rebuilt. The time required for the viscosity to recover its initial value was defined as the recovery time.

The scaffolds were produced using a 2040 Delta Turbo printer (Wasp, Massa Lombarda, Italy). The ink was extruded through a syringe equipped with a conical nozzle measuring 410 µm in diameter (Nordson EFD, Westlake, OH, USA) using compressed air in the range of 3–4 bar. The process was performed at room temperature. A plastic plate was utilized as substrate for the deposition of the scaffolds, with a thin layer of sunflower oil on the top, to facilitate their removal from the substrate. After printing, the scaffolds were left to

dry for two days at room temperature in the air. The heat treatment in static air comprised preceramic polymer cross-linking at 250 °C for 1 h, followed by ceramization for 3 h at 550 °C, 1 h at 650 °C, 3 h at 850 °C, and finally 3 h at 1300 °C. The heating rate was set at 0.5 °C/min for all steps.

Shrinkage after ceramization and sintering was measured on a preliminary set of samples (casted cubes of 10 × 10 × 10 mm^3). The measurement of the linear shrinkage in x, y, and z directions was performed using a digital caliper with a resolution of 0.01 mm. Following the output of shrinkage measurements (Figure 1b), parallelepiped scaffolds were manufactured with a post-sintering size of 10 × 10 × 4 mm^3, resulting from the overlapping of 12 layers of cylindrical rods, periodically arranged along the *x* and *y* axes, with successive layers perpendicular to each other. The distance between two continuous parallel rods in the same layer was set at 0.7 mm, and the layer thickness at 0.35 mm. This set of samples (15) was designed for microstructural and mechanical characterization.

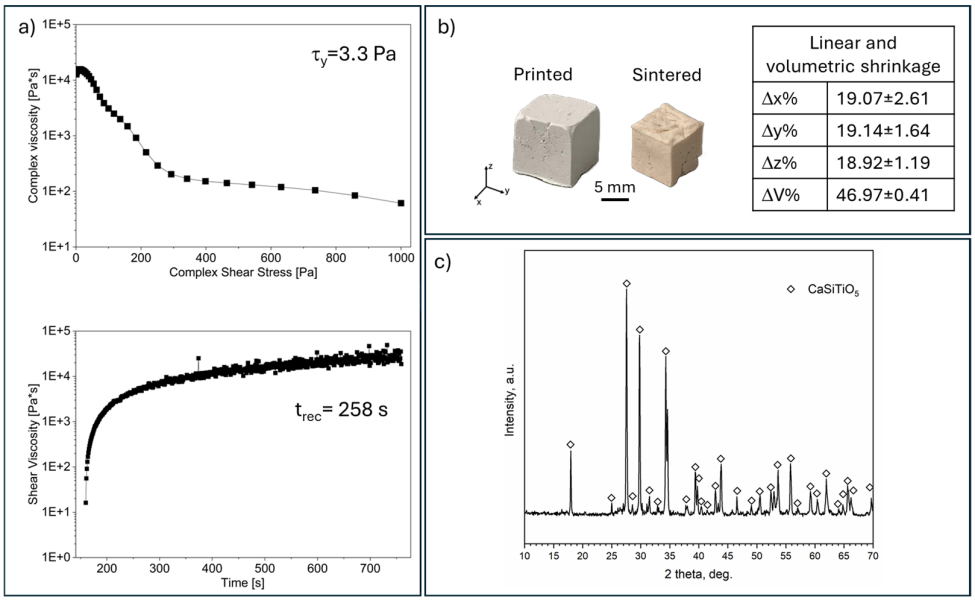

Figure 1. (**a**) Rheological properties of the DIW-printed silicone-based ink; (**b**) linear and volumetric shrinkage of the printed and sintered sphene scaffolds; (**c**) XRD diffractogram of the sintered sphene scaffolds.

For the in vivo study, cylindrical scaffolds, with post-sintering dimensions of 5 mm in diameter and 2.3 mm in height, were printed to match the morphology of the critical-size calvarial bone defect.

2.2. Scaffold Characterization

The sintered scaffolds were visually analyzed using optical stereomicroscopy (AxioCamERc 5s Microscope Camera, Carl Zeiss Microscopy, Thornwood, NY, USA). For microstructural characterization, the scaffolds were examined by scanning electron microscopy (FEI Quanta 200 ESEM, Eindhoven, The Netherlands).

X-ray diffraction (XRD) patterns of powdered scaffolds, after heat treatment, were collected with an X-ray diffractometer (Bruker AXS D8 Advance, Karlsruhe, Germany). The XRD data were analyzed using dedicated software (Match! Crystal Impact GbR version 4, Bonn, Germany), supported by data from PDF-2 database (ICDD—International Centre for Diffraction Data, Newtown Square, PA, USA).

The open porosity (P_{open}, %) of the sintered scaffolds was calculated according to the following equation:

$$P_{open} = [1 - (\rho_{bulk}/\rho_{app})] \cdot 100$$

where ρ_{bulk} is the bulk density of sphene scaffold, calculated as the ratio between the weight to the volume of the whole scaffolds, and ρ_{app} is the apparent density of the whole scaffolds, evaluated using a gas pycnometer (He, Micromeritics AccuPyc 1330, Norcross, GA, USA). The true density was determined using the He gas pycnometer on fine powders after grinding the scaffolds.

The compressive strength of the sphene scaffolds, after the heat treatment in air at 1300 °C, was measured at room temperature using a universal testing machine (Quasar 25, Galdabini S.p.a., Cardano al Campo, Italy), operating with a crosshead speed of 0.5 mm/min. The loading condition was perpendicular to the printing plane. For the physico-mechanical data, each data point represents the main average value of 10 individual tests.

2.3. In Vivo Experiments

This study was performed following the EU Directive 2010/63/EU and complies with the ARRIVE 2.0 guidelines [23]. It was approved by the Ethics Committee of the University of Padova and by the Italian Ministry of Health (No. 402/2019-PR).

2.3.1. Surgical Procedure

After an acclimatation period of one week at the Experimental Surgery Center of University of Padova, twenty healthy 25-week-old male Sprague Dawley rats, weighing approximately 450–550 g, underwent the surgery. All the surgeries were performed under general anesthesia, achieved through inhalations of oxygen and sevoflurane, in concentrations of 3% for induction and 1.5–2% for maintenance. A tramadol injection (5 mg/kg) for pain control was administrated 15 min before the surgery. The animals were then shaved, disinfected with povidone iodine 10% and stabilized in a supine position. A central incision was performed from the bipupillar line to the occipital line to expose the parietal bones. On each rat, a bilateral cylindrical 5 mm diameter full-thickness critical-size defect was created using a trephine bur [24,25]. The allocation sequence was generated prior to surgery using a computer-generated randomization sequence. One randomly chosen defect was filled with a 5 mm diameter sphene scaffold, while the contralateral defect was left empty (Figure S1). Primary intention healing was aided by a double layer suture (4.0 Vicryl, Ethicon, Inc., Somerville, NJ, USA). Tramadol (5 mg/kg s.c.) and Cefazolin (1 mg/kg i.m.) were administered twice a day and daily, respectively, for four days following the surgical procedure.

Animals were killed at randomly assigned time points of 4 and 8 weeks postoperatively (10 rats at each time point) by an overdose of anesthesia. Finally, the calvariae were harvested and fixed in 4% phosphate-buffered formalin pH 7%, for the micro-CT examinations and, subsequently, for undecalcified histology.

Animals experiencing adverse events (i.e., infection of the wound, death) during the study period were excluded.

2.3.2. Micro-CT Analysis

The specimens were scanned using the metrological X-ray CT system Nikon MCT 225 (Nikon Metrology, Tring, UK). The scans were performed in a temperature-controlled environment at 20 °C (SD 0.5), using an X-ray source tension of 120 kV and current of 57 µA, acquiring X-ray projections at an exposure time of 1415 ms to obtain CT reconstructions with a voxel size of 9 µm. The software CT Pro 3D 554 820 (Nikon Metrology, Tring, UK) was utilized for 3D reconstruction, while VGStudio MAX (Volume Graphics GmbH, Heidelberg, Germany) was used for elaboration and analysis (Figure S2).

All the analyses were performed by a single operator (G.B.) using a semi-automatic segmentation approach to minimize operator-dependent variability. A local-adaptive thresholding algorithm was used to distinguish scaffold (high radiopacity), bone (intermediate),

and soft tissue/air (low). Cutoffs were based on representative regions of interest (ROIs) and applied consistently within each dataset.

For each defect, a cylindrical ROI with a 5 mm diameter was defined at the defect. The height of each ROI was automatically set by digitally closing the defect modeling the surrounding calvarial bone surface. In the scaffold group, the scaffold volume was first digitally removed. Bone volume fraction (bone volume/total volume, BV/TV) was then calculated within the residual volume. The same analysis was performed for the empty defects. Additionally, two concentric cylindrical sub-ROIs were defined within each defect, an inner cylinder (2.5 mm diameter) and an outer ring (5 mm cylinder excluding the inner 2.5 mm), allowing for spatial evaluation of the same parameter in the two sub-ROIs (i.e., BV/TVint and BV/TVext, respectively).

The bone volume grown below and above the 5 mm diameter ROIs utilized for BV/TV calculation was measured and hereafter identified as vertical bone volume (BVvert). The quantification of bone formation extending beyond the reconstructed original skeletal envelope was assessed as an indicator of the scaffold's potential to support extraskeletal bone formation and vertical bone augmentation [4].

2.3.3. Histological Analyses

For undecalcified histology, the bone biopsies previously fixed in formalin were dehydrated in an ascending series of alcohols (i.e., 70°, 80°, 90°, and 100°) and embedded in glycol-methacrylate resin (Technovit 7200 VLC, Kulzer, Wehrheim, Germany).

The specimens were sectioned perpendicular to the calvaria surface, in the central portion of the defects to display the area showing the largest diameter with a high precision diamond disk at about 150 µm and ground down to about 70 µm with a specially designed grinding machine (Precise 1 Automated System, Assing, Rome, Italy). One slice was obtained from each specimen and subsequently stained with acid fuchsin and toluidine blue before the histological analysis.

All histological analyses were conducted using a light microscope (Laborlux S, Leitz, Wetzlar, Germany) connected to a high-resolution video camera (3CCD, JVCKY-F55B, JVC, Yokohama, Japan) and interfaced with a monitor connected to a computer. This optical system was associated with a digitizing pad (Matrix Vision GmbH, Oppenweiler, Germany) and a software package with image capturing capabilities (Image-Pro Plus 4.5, Media Cybernetics Inc., Immagini & Computer Snc, Milano, Italy). Descriptive qualitative histological evaluations were performed. In addition, the thickness of the newly formed bone close to the edges of the defects was evaluated. An illustration of measurements is provided in Figure S3.

2.4. Statistical Analyses

Statistical analyses were carried out using the open-source software R 3.3 (R Foundation for Statistical Computing, Vienna, Austria) and SPSS 28.1.1 software (SPSS Inc., Chicago, IL, USA).

Mean values and standard deviation were used for descriptive statistics, and bar graphs were used to graphically present the data.

Regarding in vivo investigation, to the best of our knowledge, there was no available study evaluating the effect of 3D-printed sphene scaffolds on new bone formation; therefore, sample size calculation was based on reasonable assumptions from similar studies utilizing the rat calvaria critical-size defect model (32–35). A sample size of 10 animals was calculated to demonstrate a mean difference of 15% in micro-CT BV/TV between test and control side after 4 weeks of healing, with a probability of type 1 error of 0.05 and a power of 80%. An additional sample size of 10 animals was calculated to demonstrate a mean difference of

30% in micro-CT BV/TV between test and control side after 8 weeks of healing, with a probability of type 1 error of 0.05 and a power of 80%. The site was considered the unit of analyses. Normality of quantitative variables, homogeneity of variance, and sphericity assumptions for repeated measures ANOVA were formally tested and met. For quantitative variables, box plots and Shapiro–Wilk tests were used to evaluate the normal distribution. Histomorphometric outcomes were compared using the paired samples *t*-test between the two groups, while the unpaired samples *t*-test was used to compare the two time points. Bonferroni's correction was performed. Micro-CT outcomes were compared through the repeated measures ANOVA test, with Bonferroni's correction. Results were considered significant with $p < 0.05$. The parameter BVvert did not satisfy the normality assumption; therefore, Wilcoxon and Mann–Whitney U tests were utilized for intra- and inter-group comparisons, respectively.

3. Results

3.1. Scaffold Production and Characterization

The rheological properties of the ink showed typical shear thinning behavior with low yield stress (3.3 Pa), high zero-shear rate viscosity (22,694.31 Pa·s) and adequate recovery time to avoid slumping of the structure after printing (258 s) (Figure 1).

Three-dimensional parallelepiped scaffolds with highly porous structure and interconnective macropores were successfully manufactured according to our computer-aided design (CAD) geometry. The sintered crack-free scaffolds exhibited a uniform, highly regular structure, as demonstrated by optical stereomicroscopy (Figure 2a) and SEM images (Figure 2b,c), with a porous structure with channels of approximately 500 × 500 µm section and length equal to the scaffold's thickness.

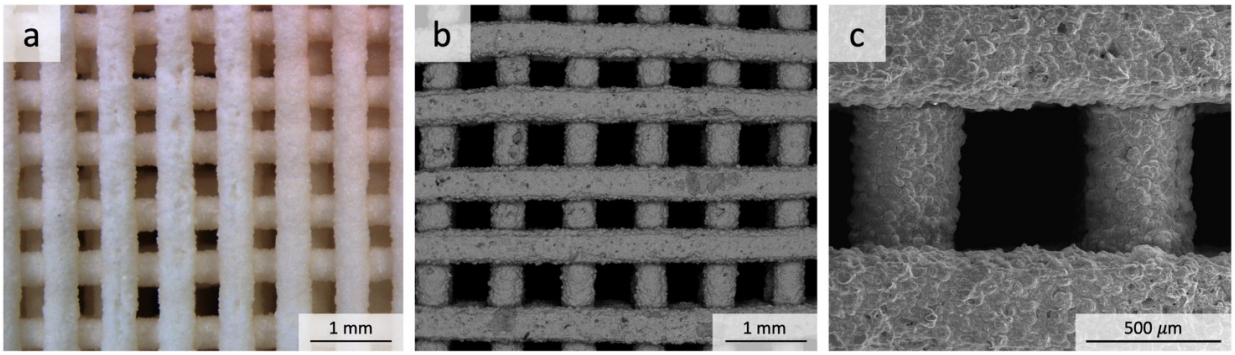

Figure 2. Top view (x-y plane) of sintered parallelepiped sphene scaffold: (**a**) optical stereomicroscope image; (**b**,**c**) SEM images at two different magnifications.

The sphene cylindrical scaffolds printed and sintered for in vivo tests show pores with a rectangular geometry of halved size in the y-z direction compared to those of the parallelepiped scaffolds. On the x-z plane the printing profile drove to closed curvatures at the edge of the cylinders (Figure 3). However, the scaffolds possessed interconnected pores that allowed them to provide suitable support for bone tissue regeneration [26].

Complete sphene crystalline phase purity was achieved after heat treatment for 3 h at 1300 °C (Figure 1c) [21].

Regarding physical characterization, the sintered scaffolds presented a bulk density (ρ_{bulk}) of 1.49 g/cm^3 (SD 0.06), an apparent density (ρ_{app}) of 3.21 g/cm^3 (SD 0.01), a true density (ρ_{true}) of 3.32 g/cm^3 (SD 0.01), an open porosity (P_{open}) of 53.71% (SD 1.98) and a total porosity of 55.22% (SD 1.92). The compressive strength (σ_{comp}) of the sintered scaffolds was 17.91 MPa (SD 4.6).

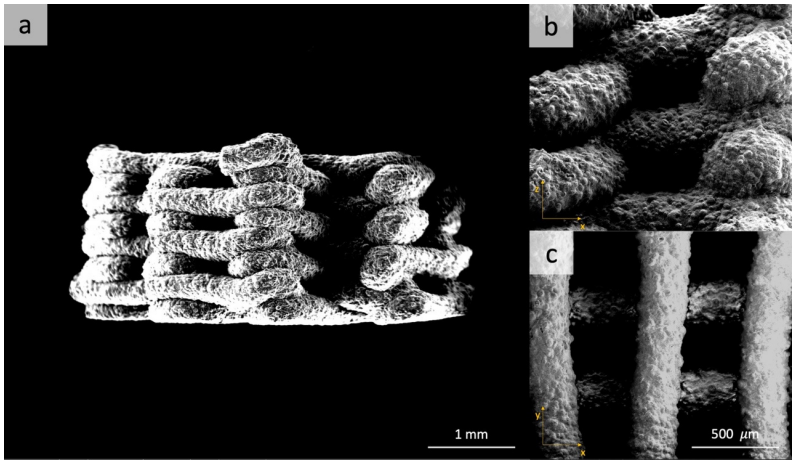

Figure 3. SEM images of sintered cylindrical scaffolds used for in vivo tests: (**a**) the whole geometry on the x-z plane; (**b**) detail of the porous geometry on the x-z plane; (**c**) detail of the geometry on the x-y plane.

3.2. In Vivo Experiments

No adverse event occurred during the surgery and the healing phase, and all animals arrived to the endpoint. Therefore, all the study animals were included in the analysis.

3.2.1. Micro-CT Analysis

Overall, BV/TV tended to increase over time in both groups up to approximately 40%, despite no statistically significant differences that could be found among the groups and the time points (Figures 4, S4 and S5, Table S1). Within the two time points, the BV/TV values were significantly higher in the external portion of the defects (BV/TVext) both in the test and control groups, as compared to the internal ones (BV/TVint) (Figures 5 and S6–S9). The *p* values obtained from the post hoc test were <0.001.

The analysis of BVvert demonstrated that the amount of newly formed bone exceeding the initial cortical layout was significantly higher in the sphene group at both time points (Table 1).

Table 1. BVvert values (mm^3).

Time Point	Group	BVvert (mm^3) [Mean (SD)]	*p* Value
4 weeks	**Sphene**	3.07 (2.70)	0.013
	Empty	1.28 (1.87)	
8 weeks	**Sphene**	1.93 (1.63)	0.013
	Empty	0.63 (0.72)	

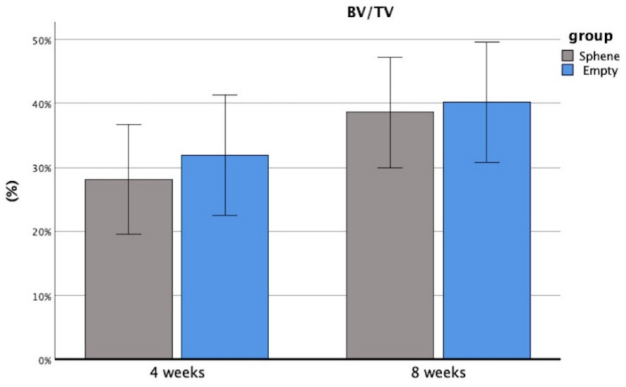

Figure 4. BV/TV. Mean and 95% confidence interval (95% CI) values are reported. Error bars: 95% CI.

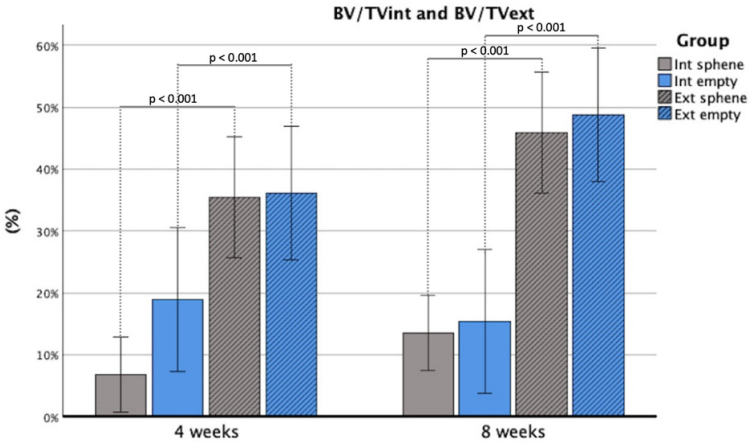

Figure 5. BV/TVint and BV/TVext. Mean and 95% confidence interval (95% CI) values are reported. Error bars: 95% CI.

3.2.2. Histological Analyses

The bone response of the 3D-printed sphene ceramic scaffolds was evaluated by histological analyses. In the sphene group, an increase in cortical bone thickness was observed at the defect margins (Figure 6a). Additionally, new bone formation was present within the pores of the scaffold, near the marginal portions of the defects (Figure 6b,c). In the control group, a thin layer of newly formed bone was present only at the margins of the defects (Figure 6d).

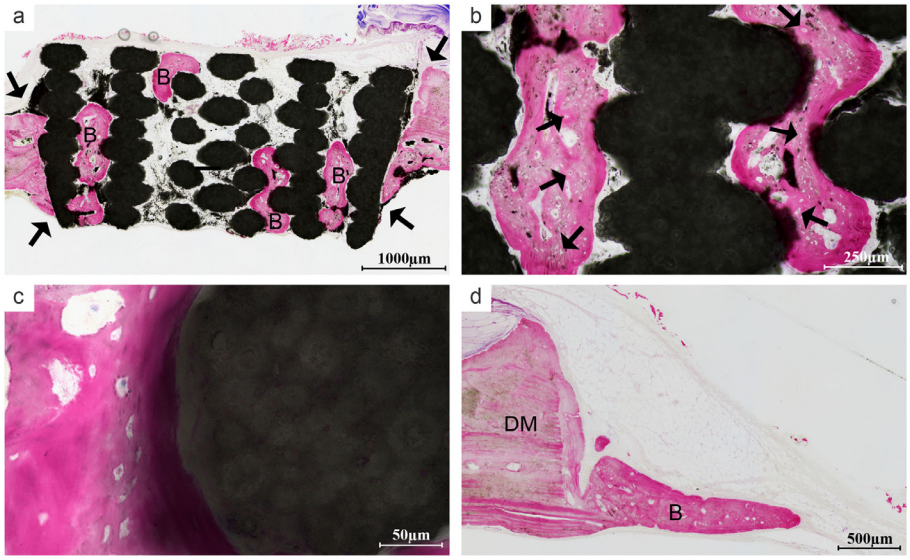

Figure 6. (**a**) Increased bone thickness is observed at the inner and outer edges of the sphene scaffold (black arrows). Within the porous structure, new bone formation (B) was observed starting from the defect margins (acid fuchsin/toluidine blue 20×). (**b**) The newly formed bone within the residual scaffold showed large osteocyte lacunae (black arrows) (acid fuchsin/toluidine blue 100×). (**c**) Interface bone/scaffold (acid fuchsin/toluidine blue 400×). (**d**) A thin layer of newly formed bone (B) was observed starting from the defect margin (DM) (acid fuchsin/toluidine blue 40×).

Details on the mean newly formed bone thickness at the internal and external margins of the defects are provided in Figures 7, 8, S10–S13 and in Table S2. The mean newly formed bone height was higher in the test group after both 4 and 8 weeks. Interestingly, when the defect was filled with the sphene scaffold, both internal and external newly formed bone were constant within the two time points, while a reduction in marginal bone height

between 4 and 8 weeks was found in the control group. After 8 weeks, differences were found between the groups, both for internal ($p = 0.04$) and external ($p < 0.001$).

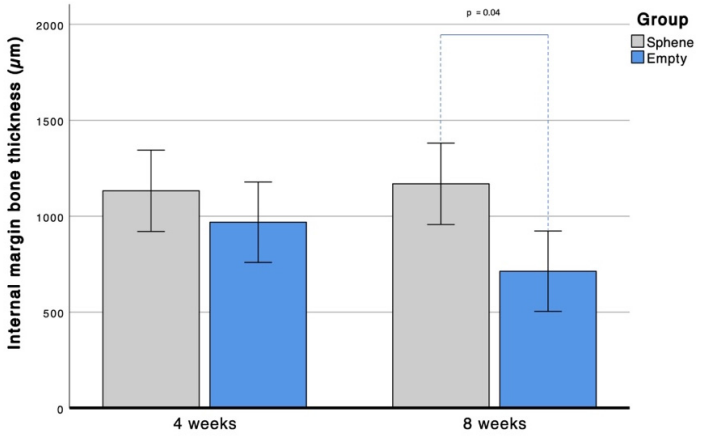

Figure 7. Measurements of internal margin bone thickness. Mean and 95% confidence interval (95% CI) values are reported. Error bars: 95% CI.

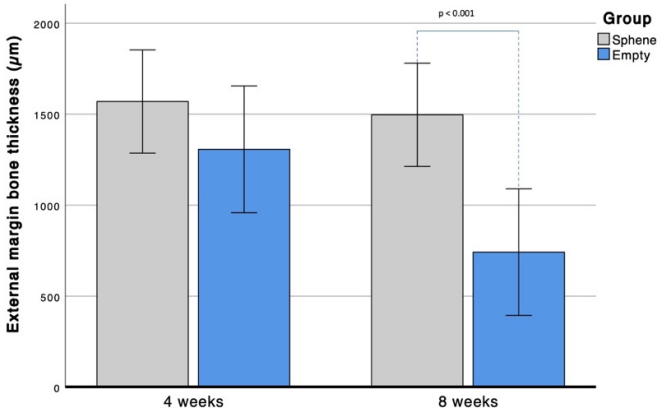

Figure 8. Measurements of external margin bone thickness. Mean and 95% confidence interval (95% CI) values are reported. Error bars: 95% CI.

4. Discussion

This in vivo study investigated the bone response of 3D-printed sphene ceramic scaffolds in a rat critical-size calvarial defect model, with empty defects serving as controls. A combination of micro-CT and undecalcified histological analysis provided complementary insights, enabling a comprehensive evaluation of the spatial distribution and morphological characteristics of newly formed bone at four and eight weeks of healing.

The use of micro-CT to quantify the amount of bone ingrowth inside porous structures was already proposed in the literature [27,28]. Here we applied micro-CT analysis to quantify the bone volume over total volume ratio, in test and control groups, with the aim of identifying the effect of the produced scaffolds on new bone formation. While micro-CT did not reveal statistically significant differences in BV/TV between groups or time points, a consistent trend was observed, with BV/TV gradually increasing over time in both groups. BV/TV values were significantly higher in the outer portion of the defect compared to the central region at each time point. Moreover, histological evaluation revealed new bone formation in direct contact with the scaffold, further supporting the biocompatibility of the material, with no evidence of inflammation or adverse tissue reactions. When focusing on the interface with the native bone surrounding the defect, histological analysis revealed a greater mean height of newly formed bone in the scaffold

group compared to the control group at both time points. The scaffolds supported vertical bone formation at the defect margins, with newly formed bone closely integrating with and adapting to the complex three-dimensional geometry of the scaffolds. However, a reduction in bone height was observed in the control group at 8 weeks, probably due to the physiological bone remodeling process [29].

The rat calvarial critical-size defect model is a well-established and reproducible model for evaluating osteoconductive biomaterials [25]. In our study, the combination of the scaffold's structural integrity and inherent bioactivity likely facilitated bone growth, particularly at the defect's periphery. Also, Yang et al. [30] conducted a spatial analysis to better understand patterns of bone regeneration. Using a concentric sub-region approach to measure bone volume fraction, they demonstrated that the architecture of 3D-printed bioceramic scaffolds plays a crucial role in directing bone ingrowth. In detail, certain designs favored peripheral bone formation, while others promoted regeneration more centrally. Consistent with these findings, our scaffold appeared to encourage greater bone formation at the periphery than in the center, suggesting that its structural configuration may have limited bone growth within the core of the defect.

Sphene ($CaTiSiO_5$) is a bioactive silicate ceramic that combines favorable mechanical and biological properties. Compared to other bioceramics such as hydroxyapatite and tricalcium phosphate, sphene exhibits higher mechanical strength and improved fracture resistance, making it an appealing candidate for applications requiring structural support in addition to biological performance [31].

The bone regeneration observed in the present in vivo calvarial model aligns well with previous in vitro findings from our group [32], where sphene granules, derived from crushing of sphene foam blocks as well as from 3D-printed scaffolds produced with the same method as here, demonstrated excellent biocompatibility and osteogenic potential. The sphene granules supported osteoblast proliferation and migration, and were associated with a sustained release of silicon ions, which are known to stimulate osteogenic activity [33]. The in vivo performance of intact sphene scaffolds of the current study, characterized by new bone formation, scaffold colonization, and integration, corroborates the bioactive behavior observed in vitro using sphene granules [32]. Further evidence supporting the potential of sphene in bone regeneration, albeit in composite form, was recently presented by Kouhi et al. [34], who incorporated sphene into 3D-printed polycaprolactone (PCL) scaffolds further modified with a zein and ZnO nanoparticle coating. Although the scaffolds did not consist of pure sphene, they supported in vitro osteogenic responses indicative of bone regeneration potential.

Another key feature of the present study was the use of Direct Ink Writing (DIW) as the fabrication technique [20,21]. DIW allowed us to produce scaffolds with controlled architecture and porosity, which are essential parameters for tissue ingrowth and vascular infiltration. Moreover, this technique enables customization of scaffold geometry to match patient-specific defect sites, making it highly suitable for personalized regenerative medicine [14]. The successful use of DIW to print sphene scaffolds confirms the feasibility of combining bioactive ceramics with advanced manufacturing technologies.

Despite the promising results, this study has some limitations that should be acknowledged. First, 3D-printed scaffolds with a porosity slightly above 50% were used, providing sufficient structural integrity. However, the scaffolds featured a relatively closed peripheral configuration. A more open design at the sides, higher porosity, together with a hierarchical architecture mimicking the cortical–cancellous bone transition, might have better promoted cell migration, vascular infiltration, and centripetal tissue formation [35,36]. While larger pores can reduce mechanical properties [37], high compression strength was not required in this non-load-bearing model. The effects of the scaffolds were largely confined to vertical

bone formation at the defect margins, with BV/TV values within the defects comparable to the control group. These findings suggest that the scaffolds primarily support localized bone regeneration rather than inducing bone formation at a distance, even though previous in vivo studies have shown the release of calcium and silicium in the solution [32]. Although bilateral defects were created in the same animal, potential crosstalk effects between the test and control sides are likely to be minimal.

Second, micro-CT analysis was performed only ex vivo at the study endpoints. While this approach provides high-resolution structural information, it does not capture the dynamic process of healing over time. Incorporating longitudinal in vivo imaging in future studies would help elucidate the dynamics of bone healing and scaffold remodeling over time. Automated 3D-2D registration of micro-CT with histological sections could further improve the analyses [38], validating the micro-CT segmentation against histological findings. Moreover, blinded assessment could not be performed, as the two groups were readily distinguishable, and power re-calculation for secondary outcome was not performed.

In conclusion, the 3D-printed sphene scaffold demonstrated good biocompatibility and supported bone formation at the periphery of critical-size calvarial defects as demonstrated by histological analysis, even though the scaffold group did not significantly outperform empty controls in the primary volumetric outcome. The favorable biological performance of sphene, combined with its mechanical stability and compatibility with DIW manufacturing, supports its potential use of this material for bone tissue engineering.

Future work should focus on refining scaffold architecture to improve internal bone ingrowth, incorporating longitudinal micro-CT evaluations to monitor healing progression, and registering micro-CT with histological sections for validation of the micro-CT segmentation. Assessment in larger animal models or load-bearing conditions could further clarify the translational potential of these scaffolds for maxillofacial applications, extending beyond small defect scenarios. Overall, the integration of sphene's biological activity with customizable DIW scaffold design may offer a compelling strategy for the development of personalized implants aimed at treating complex or large-scale bone defects.

Supplementary Materials: The following supporting information can be downloaded at https://www.mdpi.com/article/10.3390/app16073121/s1.

Author Contributions: Conceptualization: G.B., H.E., L.B. and S.S.; Data curation: G.B., H.E., L.S., E.S., G.I., L.B. and S.S.; Formal analysis: G.B., H.E., L.S., E.S. and G.I.; Investigation: G.B., H.E., L.S., E.S. and G.I.; Methodology: G.B., H.E., E.S., G.I., L.B. and S.S.; Project administration: L.B. and S.S.; Resources: L.B. and S.S.; Software: E.S. and S.C.; Supervision: B.Z., S.C., E.B., L.B. and S.S.; Visualization: G.B. and L.S.; Writing—original draft: G.B., H.E. and L.S.; Writing—review and editing: G.B., H.E., L.S., E.S., G.I., B.Z., S.C., E.B., L.B. and S.S. All authors have read and agreed to the published version of the manuscript.

Funding: This research received no external funding.

Institutional Review Board Statement: All the experimental procedures were approved by the Ethics Committee of the University of Padova and by the Italian Ministry of Health (No. 402/2019-PR).

Informed Consent Statement: Not applicable.

Data Availability Statement: The data that support the findings of this study are available from the corresponding author upon reasonable request.

Acknowledgments: The production and the characterization of the 3D-printed sphene ceramic scaffolds were performed in collaboration with Paolo Colombo (Centre for Mechanics of Biological Materials, Department of Industrial Engineering, University of Padova, Italy).

Conflicts of Interest: The authors declare no conflicts of interest.

Abbreviations

The following abbreviations are used in this manuscript:

BV/TV	bone volume/total volume
DIW	direct ink writing
micro-CT	micro-X-ray computed tomography
SEM	scanning electron microscopy
ROI	region of interest
XRD	X-ray diffraction

References

1. Buser, D.; Urban, I.; Monje, A.; Kunrath, M.F.; Dahlin, C. Guided bone regeneration in implant dentistry: Basic principle, progress over 35 years, and recent research activities. *Periodontology 2000* **2023**, *93*, 9–25. [CrossRef]
2. Tonetti, M.S.; Hämmerle, C.H.; European Workshop on Periodontology Group C. Advances in bone augmentation to enable dental implant placement: Consensus Report of the Sixth European Workshop on Periodontology. *J. Clin. Periodontol.* **2008**, *35*, 168–172. [CrossRef]
3. Urban, I.A.; Montero, E.; Monje, A.; Sanz-Sánchez, I. Effectiveness of vertical ridge augmentation interventions: A systematic review and meta-analysis. *J. Clin. Periodontol.* **2019**, *46*, 319–339. [CrossRef] [PubMed]
4. Vaquette, C.; Mitchell, J.; Ivanovski, S. Recent Advances in Vertical Alveolar Bone Augmentation Using Additive Manufacturing Technologies. *Front. Bioeng. Biotechnol.* **2021**, *9*, 798393. [CrossRef] [PubMed]
5. Merli, M.; Merli, I.; Raffaelli, E.; Pagliaro, U.; Nastri, L.; Nieri, M. Bone augmentation at implant dehiscences and fenestrations. A systematic review of randomised controlled trials. *Eur. J. Oral Implantol.* **2016**, *9*, 11–32. [PubMed]
6. Myeroff, C.; Archdeacon, M. Autogenous bone graft: Donor sites and techniques. *J. Bone Jt. Surg.* **2011**, *93*, 2227–2236. [CrossRef]
7. Shalash, M.A.; Rahman, H.A.; Azim, A.A.; Neemat, A.H.; Hawary, H.E.; Nasry, S.A. Evaluation of horizontal ridge augmentation using beta tricalcium phosphate and demineralized bone matrix: A comparative study. *J. Clin. Exp. Dent.* **2013**, *5*, e253–e259. [CrossRef]
8. Dimitriou, R.; Jones, E.; McGonagle, D.; Giannoudis, P.V. Bone regeneration: Current concepts and future directions. *BMC Med.* **2011**, *9*, 66. [CrossRef]
9. Otsuki, B.; Takemoto, M.; Fujibayashi, S.; Neo, M.; Kokubo, T.; Nakamura, T. Pore throat size and connectivity determine bone and tissue ingrowth into porous implants: Three-dimensional micro-CT based structural analyses of porous bioactive titanium implants. *Biomaterials* **2006**, *27*, 5892–5900. [CrossRef]
10. Abdelaziz, A.G.; Nageh, H.; Abdo, S.M.; Abdalla, M.S.; Amer, A.A.; Abdal-Hay, A.; Barhoum, A. A Review of 3D Polymeric Scaffolds for Bone Tissue Engineering: Principles, Fabrication Techniques, Immunomodulatory Roles, and Challenges. *Bioengineering* **2023**, *10*, 204. [CrossRef]
11. Serrano-Aroca, Á.; Cano-Vicent, A.; Serra, S.R.I.; El-Tanani, M.; Aljabali, A.; Tambuwala, M.M.; Mishra, Y.K. Scaffolds in the microbial resistant era: Fabrication, materials, properties and tissue engineering applications. *Mater. Today Bio* **2022**, *16*, 100412. [CrossRef] [PubMed]
12. Markiewicz, M.R.; Bell, R.B. Modern concepts in computer-assisted craniomaxillofacial reconstruction. *Curr. Opin. Otolaryngol. Head Neck Surg.* **2011**, *19*, 295–301. [CrossRef] [PubMed]
13. Oka, K.; Murase, T.; Moritomo, H.; Goto, A.; Sugamoto, K.; Yoshikawa, H. Corrective osteotomy using customized hydroxyapatite implants prepared by preoperative computer simulation. *Int. J. Med. Robot. Comput. Assist. Surg.* **2010**, *6*, 186–193. [CrossRef] [PubMed]
14. Nayak, V.V.; Slavin, B.V.; Bergamo, E.T.P.; Torroni, A.; Runyan, C.M.; Flores, R.L.; Kasper, F.K.; Young, S.; Coelho, P.G.; Witek, L. Three-Dimensional Printing Bioceramic Scaffolds Using Direct-Ink-Writing for Craniomaxillofacial Bone Regeneration. *Tissue Eng. Part C Methods* **2023**, *29*, 332–345. [CrossRef]
15. Yuan, H.; Xing, K.; Hsu, H.Y. Trinity of Three-Dimensional (3D) Scaffold, Vibration, and 3D Printing on Cell Culture Application: A Systematic Review and Indicating Future Direction. *Bioengineering* **2018**, *5*, 57. [CrossRef]
16. Zhang, L.; Yang, G.; Johnson, B.N.; Jia, X. Three-dimensional (3D) printed scaffold and material selection for bone repair. *Acta Biomater.* **2019**, *84*, 16–33. [CrossRef]
17. Saadi, M.; Maguire, A.; Pottackal, N.T.; Thakur, M.S.H.; Ikram, M.M.; Hart, A.J.; Ajayan, P.M.; Rahman, M.M. Direct Ink Writing: A 3D Printing Technology for Diverse Materials. *Adv. Mater.* **2022**, *34*, e2108855. [CrossRef]
18. Chen, Z.; Li, Z.; Li, J.; Liu, C.; Lao, C.; Fu, Y.; Liu, C.; Li, Y.; Wang, P.; He, Y. 3D printing of ceramics: A review. *J. Eur. Ceram. Soc.* **2019**, *39*, 661–687. [CrossRef]
19. Brunello, G.; Biasetto, L.; Elsayed, H.; Sbettega, E.; Gardin, C.; Scanu, A.; Carmignato, S.; Zavan, B.; Sivolella, S. An in vivo study in rat femurs of bioactive silicate coatings on titanium dental implants. *J. Clin. Med.* **2020**, *9*, 1290. [CrossRef]

20. Elsayed, H.; Grigolato, L.; Savio, G.; Colombo, P.; Bernardo, E. Direct ink writing of silicone/filler mixtures for sphene scaffolds with advanced topologies. *Int. J. Appl. Ceram. Technol.* **2023**, *20*, 131–140. [CrossRef]
21. Elsayed, H.; Sayed, M.; Naga, S.M.; Rebesan, P.; Gardin, C.; Zavan, B.; Colombo, P.; Bernardo, E. Additive manufacturing and direct synthesis of sphene ceramic scaffolds from a silicone resin and reactive fillers. *J. Eur. Ceram. Soc.* **2022**, *42*, 286–295. [CrossRef]
22. Paquien, J.-N.; Galy, J.; Gérard, J.-F.; Pouchelon, A. Rheological studies of fumed silica–polydimethylsiloxane suspensions. *Colloids Surf. A Physicochem. Eng. Asp.* **2005**, *260*, 165–172. [CrossRef]
23. Percie du Sert, N.; Hurst, V.; Ahluwalia, A.; Alam, S.; Avey, M.T.; Baker, M.; Browne, W.J.; Clark, A.; Cuthill, I.C.; Dirnagl, U.; et al. The ARRIVE guidelines 2.0: Updated guidelines for reporting animal research. *BMJ Open Sci.* **2020**, *4*, e100115. [CrossRef] [PubMed]
24. Huang, J.; Ratnayake, J.; Dias, G.J. Critical size defect in a rat calvaria model using trephination: An animal model for investigating potential bone regenerative scaffolds. *MethodsX* **2025**, *14*, 103355. [CrossRef] [PubMed]
25. Vajgel, A.; Mardas, N.; Farias, B.C.; Petrie, A.; Cimões, R.; Donos, N. A systematic review on the critical size defect model. *Clin. Oral Implant. Res.* **2014**, *25*, 879–893. [CrossRef]
26. Gao, C.; Deng, Y.; Feng, P.; Mao, Z.; Li, P.; Yang, B.; Deng, J.; Cao, Y.; Shuai, C.; Peng, S. Current progress in bioactive ceramic scaffolds for bone repair and regeneration. *Int. J. Mol. Sci.* **2014**, *15*, 4714–4732. [CrossRef]
27. Janmohammadi, M.; Doostmohammadi, N.; Bahraminasab, M.; Nourbakhsh, M.S.; Arab, S.; Asgharzade, S.; Ghanbari, A.; Satari, A. Evaluation of new bone formation in critical-sized rat calvarial defect using 3D printed polycaprolactone/tragacanth gum-bioactive glass composite scaffolds. *Int. J. Biol. Macromol.* **2024**, *270*, 132361. [CrossRef]
28. Chen, M.C.; Chiu, H.C.; Kuo, P.J.; Chiang, C.Y.; Fu, M.M.; Fu, E. Bone formation with functionalized 3D printed poly-ε-caprolactone scaffold with plasma-rich-fibrin implanted in critical-sized calvaria defect of rat. *J. Dent. Sci.* **2021**, *16*, 1214–1221. [CrossRef]
29. Einhorn, T.A.; Gerstenfeld, L.C. Fracture healing: Mechanisms and interventions. *Nat. Rev. Rheumatol.* **2015**, *11*, 45–54. [CrossRef]
30. Yang, Z.; Wang, C.; Gao, H.; Jia, L.; Zeng, H.; Zheng, L.; Wang, C.; Zhang, H.; Wang, L.; Song, J.; et al. Biomechanical Effects of 3D-Printed Bioceramic Scaffolds With Porous Gradient Structures on the Regeneration of Alveolar Bone Defect: A Comprehensive Study. *Front. Bioeng. Biotechnol.* **2022**, *10*, 882631. [CrossRef]
31. No, Y.J.; Li, J.J.; Zreiqat, H. Doped Calcium Silicate Ceramics: A New Class of Candidates for Synthetic Bone Substitutes. *Materials* **2017**, *10*, 153. [CrossRef]
32. Sivolella, S.; Brunello, G.; Nika, E.; Badocco, D.; Pastore, P.; Carturan, S.M.; Bernardo, E.; Elsayed, H.; Biasetto, L.; Brun, P. In vitro evaluation of granules obtained from 3D sphene scaffolds and bovine bone grafts: Chemical and biological assays. *J. Mater. Chem. B* **2023**, *11*, 8775–8787. [CrossRef] [PubMed]
33. Götz, W.; Tobiasch, E.; Witzleben, S.; Schulze, M. Effects of Silicon Compounds on Biomineralization, Osteogenesis, and Hard Tissue Formation. *Pharmaceutics* **2019**, *11*, 117. [CrossRef] [PubMed]
34. Kouhi, M.; Khodaei, M.; Behrouznejad, B.; Savabi, O.; Bodaghi, M. Zein/ZnO-Modified 3D-Printed PCL/Sphene Scaffolds with Improved Bacterial Inhibition and Osteoblast Activity for Bone Regeneration Applications. *ACS Biomater. Sci. Eng.* **2025**, *11*, 2898–2909. [CrossRef] [PubMed]
35. Wu, B.; Yang, J.; Ye, J.; Chang, W.; Zhang, X.; Walsh, W.; Zhou, Y. Extrusion-based 3D printing of cross-scale porous bone scaffolds and their micro-topological structures for bone repair. *Biomater. Adv.* **2026**, *180*, 214540. [CrossRef]
36. Kim, Y.M.; Ghim, M.-S.; Quan, M.; Kim, Y.Y.; Cho, Y.-S. Experimental Verification of the Impact of the Contact Area between the Defect Site and the Scaffold on Bone Regeneration Efficacy. *Polymers* **2024**, *16*, 338. [CrossRef]
37. Sun, J.; Chen, C.; Zhang, B.; Yao, C.; Zhang, Y. Advances in 3D-printed scaffold technologies for bone defect repair: Materials, biomechanics, and clinical prospects. *Biomed. Eng. Online* **2025**, *24*, 51. [CrossRef]
38. Becker, K.; Stauber, M.; Schwarz, F.; Beißbarth, T. Automated 3D-2D registration of X-ray microcomputed tomography with histological sections for dental implants in bone using chamfer matching and simulated annealing. *Comput. Med. Imaging Graph.* **2015**, *44*, 62–68. [CrossRef]